Synthesis, Crystal Structure, Polymorphism, and Magnetism of Eu(CN$_3$H$_4$)$_2$ and First Evidence of EuC(NH)$_3$

Arno L. Görne [1], Janine George [1], Jan van Leusen [1] and Richard Dronskowski [1,2,*]

[1] Institute of Inorganic Chemistry, RWTH Aachen University, Landoltweg 1, 52056 Aachen, Germany;
arno.goerne@ac.rwth-aachen.de (A.L.G.); janine.george@ac.rwth-aachen.de (J.G.);
jan.vanleusen@ac.rwth-aachen.de (J.v.L.)

[2] Jülich-Aachen Research Alliance, JARA-HPC, RWTH Aachen University, 52056 Aachen, Germany

* Correspondence: drons@HAL9000.ac.rwth-aachen.de; Tel.: +49-(0)-241-80-93642

Abstract: We report the first magnetically coupled guanidinate, α-Eu(CN$_3$H$_4$)$_2$ (monoclinic, $P2_1$, a = 5.8494(3) Å, b = 14.0007(8) Å, c = 8.4887(4) Å, $β$ = 91.075(6)°, V = 695.07(6) Å^3, Z = 4). Its synthesis, polymorphism, crystal structure, and properties are complemented and supported by density-functional theory (DFT) calculations. The α-, β- and γ-polymorphs of Eu(CN$_3$H$_4$)$_2$ differ in powder XRD, while the γ-phase transforms into the β-form over time. In α-Eu(CN$_3$H$_4$)$_2$, Eu is octahedrally coordinated and sits in one-dimensional chains; the guanidinate anions show a hydrogen-bonding network. The different guanidinate anions are theoretically predicted to adopt *syn-*, *anti-* and all-*trans*-conformations. Magnetic measurements evidence ferromagnetic interactions, presumably along the Eu chains. Finally, EuC(NH)$_3$ (isostructural to SrC(NH)$_3$ and YbC(NH)$_3$, hexagonal, $P6_3/m$, a = 5.1634(7) Å, c = 7.1993(9) Å, V = 166.23(4) Å^3, Z = 2) is introduced as a possible ferromagnet.

**Keywords:** europium; guanidinate; DFT; IR; liquid ammonia

1. Introduction

At the beginning of the 21st century, rare-earth metals are critical materials in high-technology applications [1]. Within the recent decades, several technological innovations disrupted the rare-earth market [2], in turn stimulating the scientific quest for future materials. One vibrant field is the study of Eu^{2+} compounds whose complex crystal structures are coupled with application-relevant properties including, to name only some recent examples, luminescence [3–6], field-induced reversal of the magnetoresistive effect [7], and complex magnetism [8,9]. The most renowned magnetic compounds are the europium chalcogenides that are considered ideal 3D Heisenberg systems [10]. While EuO is a ferromagnet with a Curie temperature of 69.3 K [11–13], EuS is also a ferromagnet but with a far lower Curie temperature of 18.7 K, showing weak, secondary antiferromagnetic interactions [13].

Our interest lies in nitrogen-based materials. For Eu^{2+}, there are a number of simple amides, thiocyanates, and carbodiimides such as Eu(NH$_2$)$_2$ [14,15], Eu(NCS)$_2$ [16], and EuNCN [17], but also a growing number of more exotic and intriguing examples including Eu$_2$Si$_5$N$_8$ [18,19], Eu$_3$[NBN]$_2$ [20], Eu$_2$Cl$_2$NCN [21], and EuSi$_2$O$_2$N$_2$ [22]. Low-dimensional magnetic properties have been reported in Eu^{2+} coordination polymers with 2,2′-bipyridime showing 1D ferromagnetic interactions [23] and in LiEu$_2$(NCN)I$_3$ and LiEu$_4$(NCN)$_3$I$_3$ [24], also with low-dimensional ferromagnetic ordering and possibly conflicting antiferromagnetic interactions at very low temperatures.

Here, we present the first europium guanidinates, inorganic salts derived from the molecule guanidine CN$_3$H$_5$ [25,26]. Our group has already pioneered the deprotonation of this strongly

basic molecule (Figure 1), demonstrated by the preparation of the alkali-metal guanidinates [27–29]. Progressing from there, we recently reported *doubly* deprotonated guanidinates—in $SrC(NH)_3$ and $YbC(NH)_3$—and the first magnetic guanidinate, $Yb(CN_3H_4)_3$, a non-Curie–Weiss paramagnet [30,31]. In the following, we present the first magnetically coupled guanidinate, α-$Eu(CN_3H_4)_2$, with probable 1D ferromagnetic order. We detail its synthesis, polymorphism, crystal structure, and properties, complemented and supported by density-functional theory (DFT) calculations. Also, we present a preliminary report on $EuC(NH)_3$ and a first indication of its magnetic properties.
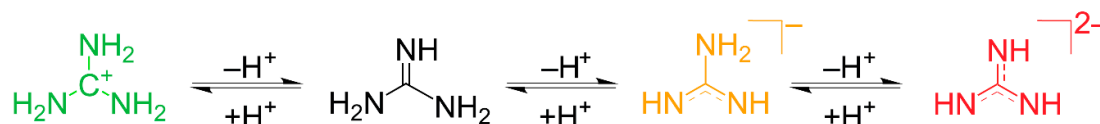

Figure 1. Protonation and deprotonation of guanidine from guanidinium on the left to the doubly deprotonated guanidinate on the right.

2. Results and Discussion

2.1. Polymorphism of Eu(CN₃H₄)₂

Depending on the synthetic conditions, three polymorphs of $Eu(CN_3H_4)_2$ could be prepared, which we call α, β, and γ. The polymorphs show different powder X-ray diffraction (PXRD) patterns (Figure 2a). For the α-phase, the crystal structure was solved (see below). α-$Eu(CN_3H_4)_2$ was prepared at temperatures around 65 °C, the β-phase at a lower 50 °C, and the γ-phase exclusively around room temperature. Under these conditions, Eu^{2+} is the stable oxidation state, and Eu^{3+} would only form at temperatures starting around 300 °C [32]. The oxidation state was also corroborated by the magnetic measurements (see Section 2.3). Interestingly, the γ-phase spontaneously transforms to the β-phase over several weeks (Figure 2b), so γ-$Eu(CN_3H_4)_2$ must be a metastable phase.
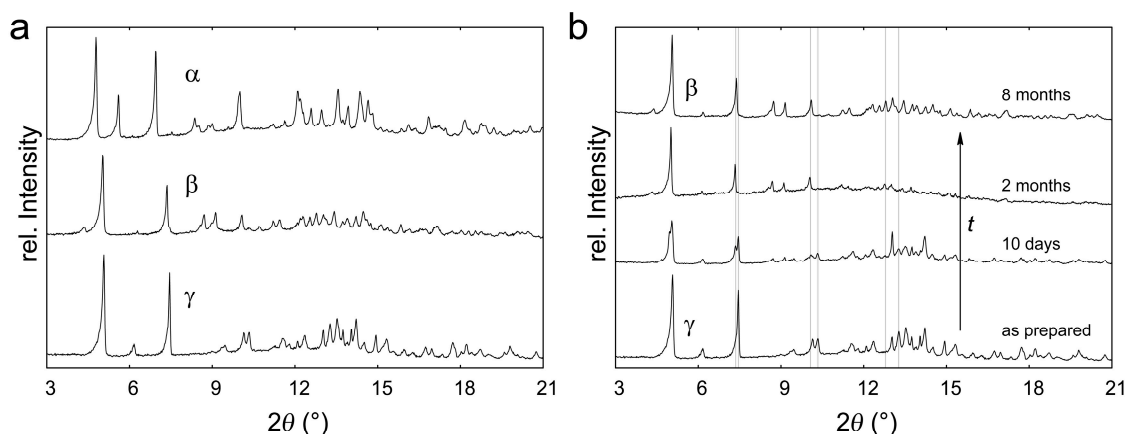
Figure 2. Diffraction patterns of the different polymorphs of $Eu(CN_3H_4)_2$ (**a**) and the transformation from the γ-phase to the β-phase over time (**b**).

IR measurements indicate a strong similarity between the α- and β-phase (Figure 3), not surprisingly so because the spectrum is dominated by the $CN_3H_4^-$ anion vibrations [31]. In addition, there is no trace of an IR contribution of the $C(NH)_3^{2-}$ unit, which supports the proposed composition. The IR spectrum of α-$Eu(CN_3H_4)_2$ was also calculated by DFT from the density of phonon states and the Born effective charges as explained in references [33] and [34]. All observed signals were reproduced, while the differing intensity of the simulated signals could be caused by a thermal effect (calculated 0 K vs experimental 300 K). To identify the vibrations, the IR-active phonons at the Γ-point were visualized (Table 1).
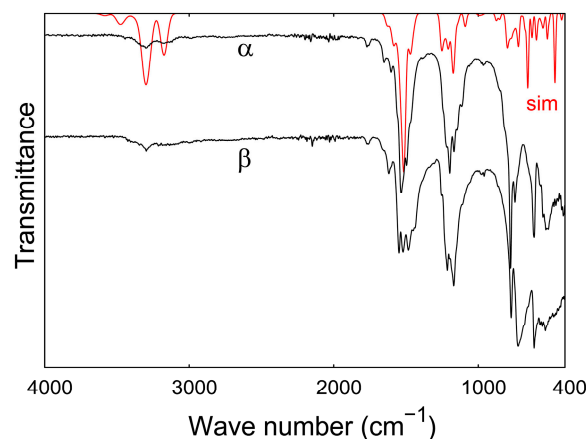
Figure 3. IR measurement of the β- (with an offset) and α-polymorphs of Eu(CN$_3$H$_4$)$_2$ and simulation of the latter.

Table 1. Assignment of vibrational bands of α-Eu(CN$_3$H$_4$)$_2$ as obtained with density-functional theory (DFT).

| Vibration	α-Eu(CN$_3$H$_4$)$_2$ (cm^{-1})
$\nu_{s,\,as}$(N–H)	3299, 3172
δ_{sciss}(N–H)	1652, 1602
ν_s, δ_{sciss}(C–N); δ_{sciss}(N–H)	1533, 1495
δ_{rock}(N–H)	1197–1167
δ_{wagg}(N–H)	1147–1114
ν_{breath}(CN$_3$)	965
δ_{twist}(N–H)	776
C-inversion by CN$_3$ plane	746
δ_{rock}(C–N), δ_{rock}(N–H)	614
δ_{sciss}(C–N), δ_{sciss}(N–H)	532–514

Preliminary thermogravimetric analysis (TGA) measurements of α- and β-Eu(CN$_3$H$_4$)$_2$ show a two-step decay. The first step around 155 °C corresponds to the loss of two equivalents of ammonia, typical for guanidinates [30,31,35], to arrive at the hydrogen cyanamide Eu(NCNH)$_2$. This phase has not been prepared before. The second step around 250 °C does not plateau in the measurement range up to 350 °C. This step could be the transformation of europium hydrogen cyanamide to the carbodiimide by releasing H$_2$NCN, as observed, for example, in the transition-metal hydrogen cyanamides of Fe, Co, and Ni [36,37]. EuNCN could not be prepared as a single-phase material in the reported synthesis at 1300 K [17]. Thus, the guanidinates appear as interesting precursor materials for new (hydrogen) cyanamides.

2.2. Refinement and Crystal Structure of α-Eu(CN$_3$H$_4$)$_2$

α-Eu(CN$_3$H$_4$)$_2$ crystallizes in the acentric, monoclinic space group $P2_1$ with a = 5.8494(3) Å, b = 14.0007(8) Å, c = 8.4887(4) Å, β = 91.075(6)°, V = 695.07(6) Å^3, and Z = 4 (Table 2). The asymmetric unit consists of two Eu atoms and four independent guanidinate units. The large number of parameters, the limited number of reflections, and the domination of the X-ray scattering by the heavy Eu atoms required a number of restraints and constraints to obtain a reasonable structure: while the Eu atoms were refined anisotropically, the C and N atoms of each guanidinate unit were constrained to a single U_{iso} value. Also, the C–N bond lengths, N–C–N angles, and CN$_3$ torsion angles were restrained to sensible values (as obtained from similar guanidinates in the literature). The obtained structural model fits the PXRD measurement well (Figure 4). Different C–N bond lengths allowed for a distinction between amine and imine groups, while the assignment was confirmed by the DFT calculations. In addition, we detected a minor side phase of EuO, likely formed during handling of Eu metal under

argon. Such an impurity can often be seen in the literature [38]. The Rietveld refinement estimates the amount of EuO as 1.3(2) wt %.
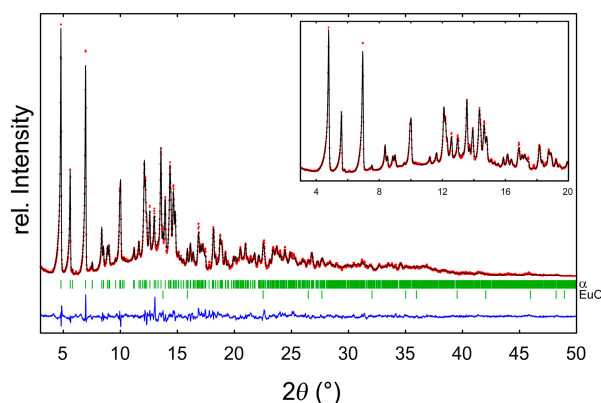
Figure 4. Rietveld refinement of α-Eu(CN$_3$H$_4$)$_2$ with a minor side phase of EuO measured with Mo $K\alpha_1$ radiation.

Table 2. Crystallographic data and refinement details for EuC(NH)$_3$ and α-Eu(CN$_3$H$_4$)$_2$.

Formula	α-Eu(CN$_3$H$_4$)$_2$	EuC(NH)$_3$
Formula weight (g·mol^{-1})	268.09	209.02
Crystal system	Monoclinic	Hexagonal
Space group	$P2_1$ (Nr. 4)	$P6_3/m$ (Nr. 176)
Temperature (K)	298	298
a (Å)	5.8494(3)	5.1634(7)
b (Å)	14.0007(8)	$= a$
c (Å)	8.4887(4)	7.1993(9)
β (°)	91.075(6)	90
V (Å^3)	695.07(6)	166.22(4)
Z	4	2
Cryst. density (g·cm^{-3})	2.4848(2)	4.1176(9)
Radiation	Mo $K\alpha_1$	Mo $K\alpha_1$
No. reflections	870	108
No. restraints/constraints	24/4	0/1
No. refined parameters	71	14
R_P, wR_P[a]	3.7/4.9	5.1/7.3
R_Bragg, R_F[b]	11.3/6.8	18.7/11.7

[a] $R_\mathrm{P} = \frac{\sum|y(\mathrm{obs})-y(\mathrm{calc})|}{\sum y(\mathrm{obs})} \times 100$; $wR_\mathrm{P} = \sqrt{\frac{\sum w(y(\mathrm{obs})-y(calc))^2}{\sum wy(\mathrm{obs})^2}} \times 100$

[b] $R_\mathrm{Bragg} = \frac{\sum|I_{obs}-I_{calc}|}{\sum|I_{obs}|} \times 100$; $R_F = \frac{\sum|F_{obs}|-|F_{calc}|}{\sum F_{obs}} \times 100$

Neutron diffraction experiments—to improve the structural model and to localize the hydrogen atoms—were not feasible owing to the high neutron absorption of Eu. Synchrotron PXRD measurements degraded the sample visibly and led to a color change from yellow to black. The obtained diffractograms were of poor quality, something which was also observed for long measurements of β- and γ-Eu(CN$_3$H$_4$)$_2$ with our in-house X-ray diffractometer. For that reason, the crystal structures of β- and γ-Eu(CN$_3$H$_4$)$_2$ could not be determined, very unfortunately.

Thus, we used our structural model of α-Eu(CN$_3$H$_4$)$_2$ as the starting point for DFT calculations, the ultima ratio in this difficult case. First, we began with full structural optimizations and tests for dynamic stability to evaluate the plausibility of our structural model. To that end, the hydrogen positions were varied such as to find the energetically most stable structure for further phonon calculations. We will come back to the variation of the hydrogen positions below. The resulting

structure shows only minor differences from the experimental structure, and it is also dynamically stable (i.e., its density of phonon states does not contain significant imaginary modes). This is no surprise because dispersion-corrected DFT calculations have been shown to be a powerful tool to validate experimental molecular crystal structures [39]. The good agreement between experimental and fully optimized structure by DFT and the dynamic stability strongly support the plausibility of our experimental structure model.

In α-Eu(CN$_3$H$_4$)$_2$, the Eu atoms are coordinated 6-fold in distorted octahedra (Figure 5, Table 3). The octahedra are condensed to edge-sharing chains along the *b*-axis with short Eu–Eu distances of 3.66 and 3.77 Å, each bridged by two imine N atoms of different guanidinate units. Another guanidinate unit connects the corners of two octahedra via its N–C–N core, tilting the octahedra towards each other. This motif of two Eu octahedra, corresponding to the asymmetric unit, is repeated in a zigzag fashion along the chain, propagated by the 2$_1$ screw axis.
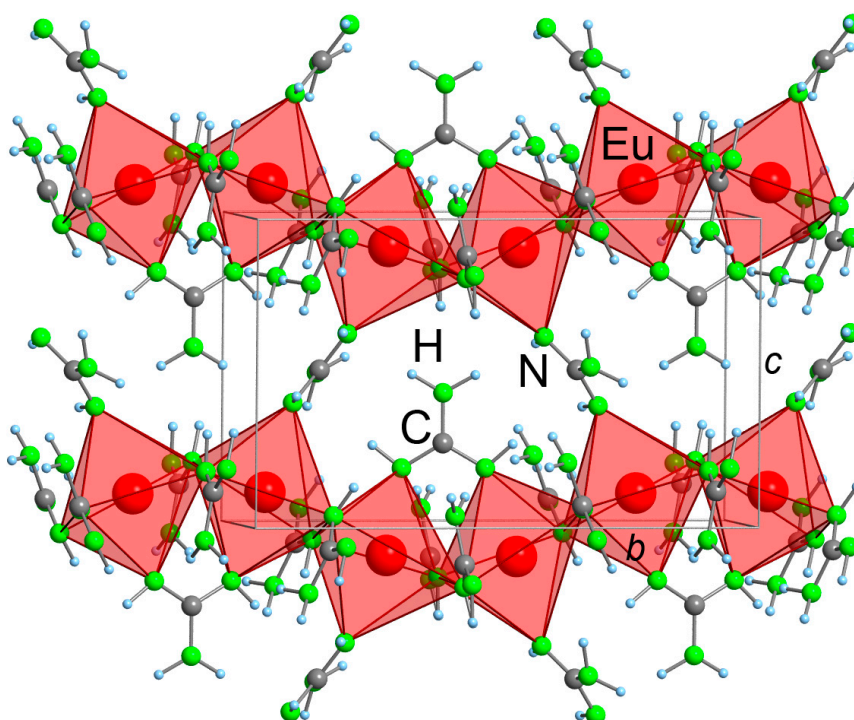

Figure 5. Crystal structure of α-Eu(CN$_3$H$_4$)$_2$ shown along the *a*-axis as optimized by DFT.

Let us return to the first guanidinate units, bridging the Eu chains by an N imine atom. The very same guanidinate units interconnect the chains along the *a*-axis, this time with the other imine N atom over their N–C–N body. Here, the Eu–Eu distance is equal to the lattice parameter *a* = 5.85 Å. Finally, along the *c*-axis, the chains are connected via the last corner of each Eu octahedron over the N–C–N body of a guanidinate with a Eu–Eu distance of 7.55 Å.
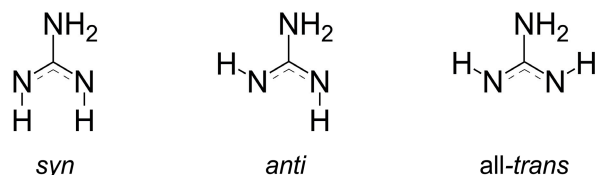
The guanidinate units are connected with each other in a hydrogen-bonding network. While other functional groups have relatively short N–H$^{\cdots}$N contacts, only those from amine to imine groups should be considered to be hydrogen-*bonded* [40].

An unusual feature of α-Eu(CN$_3$H$_4$)$_2$ is the conformation of the imine hydrogen atoms of the guanidinate units (Figure 6). In the gas phase, the most stable conformation was calculated as the *syn*-conformation [35], adopted in the solid state in KCN$_3$H$_4$, RbCN$_3$H$_4$, and CsCN$_3$H$_4$ [27,28,41]. The energetically less favorable *anti*-conformation is adopted in LiCN$_3$H$_4$ and NaCN$_3$H$_4$, owing presumably to improved packing and hydrogen-bonding [28,29]. In α-Eu(CN$_3$H$_4$)$_2$, both the *syn*- and *anti*-conformation are adopted by guanidinate units. Furthermore, one unit also adopts an all-*trans*-conformation that has never been observed before for a guanidinate. While this

conformation is unfavorable in the gas phase by 40 kJ·mol^{-1} [35], it is the predicted conformation for a hypothetical Li$^+$CN$_3$H$_4$$^-$ *ion pair* in the gas phase [29]. *Substituted* guanidinates can also adopt this conformation [42,43]. In the case of α-Eu(CN$_3$H$_4$)$_2$, this conformation is taken by the guanidinate unit connecting the motif of the two tilted Eu octahedra, and this conformational change seemingly allows for a better coordination by the imine groups.

Table 3. Atomic positions of α-Eu(CN$_3$H$_4$)$_2$ in space group *P*2$_1$ (all on Wyckoff position 2*a*) as determined from DFT.

Atom	*x*	*y*	*z*
Eu1	0.5358	0.7086	0.0995
Eu2	0.5091	0.4477	0.1043
C1	0.4778	0.5939	−0.2622
C2	0.0096	0.5851	0.1186
C3	0.9894	0.8521	0.0723
C4	0.4115	0.8357	0.5014
N1	0.4261	0.6722	−0.1801
N2	0.5249	0.5123	−0.1822
N3	0.4775	0.5942	−0.4249
N4	0.2256	0.5851	0.1783
N5	−0.1886	0.5721	0.1963
N6	−0.0171	0.6030	−0.0391
N7	0.8237	0.8338	−0.0357
N8	1.2141	0.8350	0.0569
N9	0.9070	0.8881	0.2132
N10	0.5037	0.7872	0.3822
N11	0.5109	0.8953	0.6061
N12	0.1747	0.8252	0.5170
H1	0.3877	0.7278	−0.2540
H2	0.5761	0.4617	−0.2613
H3	0.4914	0.6572	−0.4856
H4	0.5196	0.533	−0.4836
H5	0.2196	0.5831	0.2991
H6	−0.1546	0.5563	0.3121
H7	0.1267	0.6207	−0.1006
H8	−0.1558	0.5741	−0.0972
H9	0.8935	0.7988	−0.1291
H10	1.2891	0.8532	0.1636
H11	0.7685	0.9334	0.2022
H12	1.0256	0.9096	0.2948
H13	0.6727	0.8069	0.3758
H14	0.6814	0.8996	0.5808
H15	0.1090	0.7649	0.4674
H16	0.1149	0.8394	0.6260

Figure 6. Possible conformations for the singly deprotonated guanidinate CN$_3$H$_4$$^-$.

To further computationally test the calculated hydrogen positions and conformations, we optimized four additional cells with *anti*- or *syn*-conformation, replacing the all-*trans*-conformation. All results were energetically significantly less favorable by at least 12 kJ·mol^{-1} per formula unit of

$Eu(CN_3H_4)_2$. Thus, we consider the DFT prediction to be reliable, but eagerly wait for further experimental corroboration.

2.3. Magnetism of α-Eu(CN₃H₄)₂

Magnetic measurements of α-$Eu(CN_3H_4)_2$ were conducted with different applied magnetic fields (Figure 7). The field-dependence of the effective magnetic moment μ_{eff} at room temperature reveals a small ferromagnetic impurity: tiny fragments of the steel autoclaves contaminating the sample, described in reference [31]. The maximum at ca. 70 K further reveals traces of EuO within the sample, consistent with the Rietveld analysis. Hence, the data for $T > 20$ K were corrected as detailed in the Methods section and reference [10].
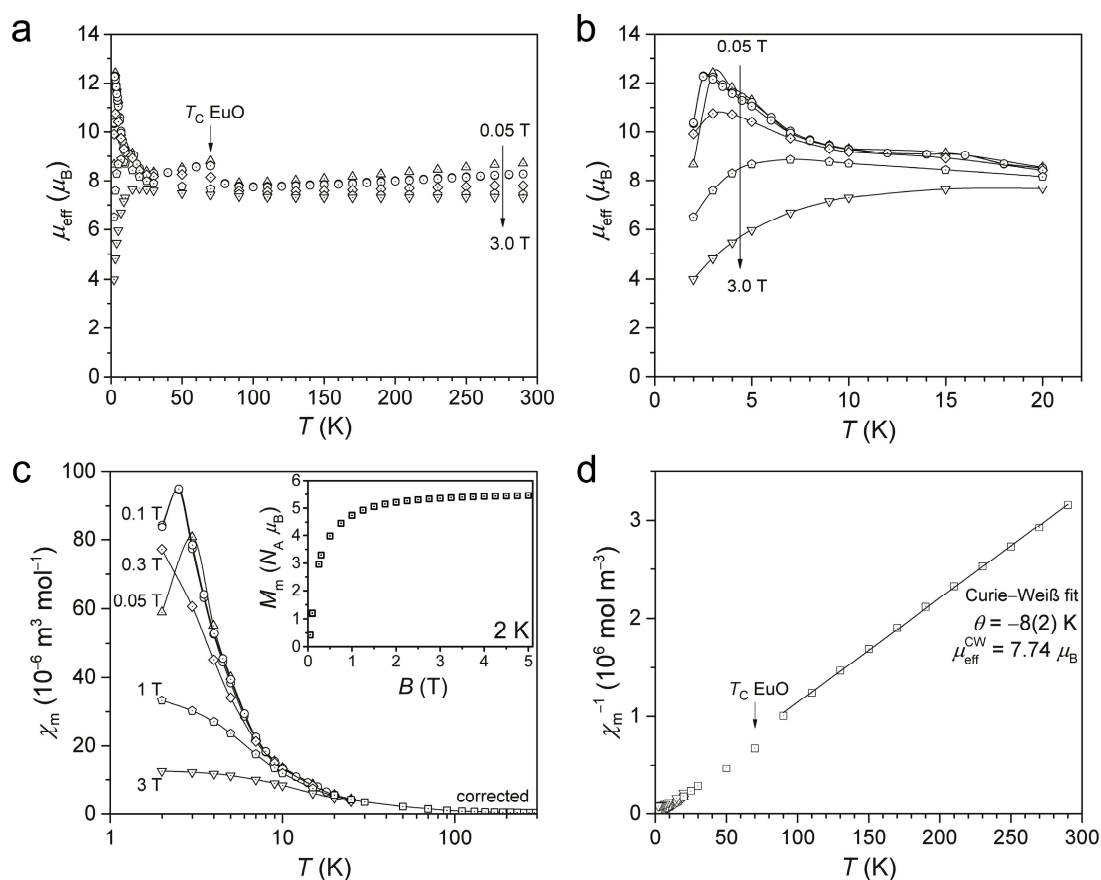
Figure 7. Effective magnetic moment (**a**) vs temperature for α-$Eu(CN_3H_4)_2$ at different applied fields; effective magnetic moment in more detail (**b**) revealing ferromagnetic exchange interactions (lines in (**b**) and (**c**) as guide to the eye only). Molar, corrected magnetic susceptibility (**c**) vs temperature for different applied fields; inset: magnetization versus applied field at 2.0 K. Corrected inverse molar susceptibility (**d**) vs temperature, and fit to the Curie–Weiss law.

At room temperature, the μ_{eff} value of noninteracting Eu^{2+} ($4f^7$, $g_J = 2$, $J = 7/2$) ions is expected to be close to 7.91 μ_B, lowered by noticeable spin-orbit coupling contributions from the spin-only value of 7.94 μ_B [44,45]. A Curie–Weiss fit of the corrected data ($T > 90$ K) gives an effective magnetic moment of 7.74 μ_B and a slightly negative Curie temperature with −8(2) K. Although both values imply antiferromagnetic exchange interactions between the Eu^{2+} ions, they should be looked at as artifacts of the correction method since exchange interactions between lanthanide centers are usually very small ($-2J < 2$ cm^{-1}).

The field-dependent molar magnetization M_m curve at 2.0 K hints at a saturation value of $M_{m,sat} \leq 6\,N_A\,\mu_B$, significantly lower than the expected saturation value of $7.0\,N_A\,\mu_B$ for noninteracting Eu^{2+} ($4f^7$) ions. The ratio of these saturation magnetizations is different from the squared ratio of the effective moments μ_{eff} at room temperature; that is, there is not a common factor that could scale both values to reach the expectation. Thus, we can conclude the existence of exchange interactions within the compound, while their nature is ambiguous. The field-dependent maxima in the μ_{eff} vs T data in the temperature range 2–6 K indicate ferromagnetic exchange interactions.

It should be noted that Eu^{3+} has a distinctly different magnetic behavior [10]: its magnetic susceptibility as a function of temperature is almost constant and hence does *not* exhibit Curie–Weiss behavior. Its high-temperature μ_{eff} value is expected to be only 3.5 μ_B, while μ_{eff} shows a strong temperature dependence. This is all in stark contrast to the magnetic measurements of α-Eu(CN$_3$H$_4$)$_2$, thus conclusively showing that Eu is in the oxidation state +2.

In summary, the low-temperature data indicate ferromagnetic exchange interactions, most likely due to one-dimensional, weak interactions along the Eu^{2+} chains of the crystal structure. Different, minor antiferromagnetic exchange pathways may additionally characterize the compound as indicated by the negative Curie temperature; they are, however, subject to speculation due to the uncertainties arising from the necessary correction for ferromagnetic impurities at $T > 20$ K.

2.4. Introduction of EuC(NH)$_3$

Finally, we want to give a preliminary account of EuC(NH)$_3$. This compound is isostructural to SrC(NH)$_3$ [30] and YbC(NH)$_3$ [31] and crystallizes in the hexagonal space group $P6_3/m$ with $a = 5.1634(7)$ Å, $c = 7.1993(9)$ Å, $V = 166.23(4)$ Å^3, and $Z = 2$ (Figure 8; Table 2). As for YbC(NH)$_3$, DFT calculations were used to locate the hydrogen atoms, a method validated in reference [46] (Table 4). So far, EuC(NH)$_3$ was only obtained together with an unidentified side phase.
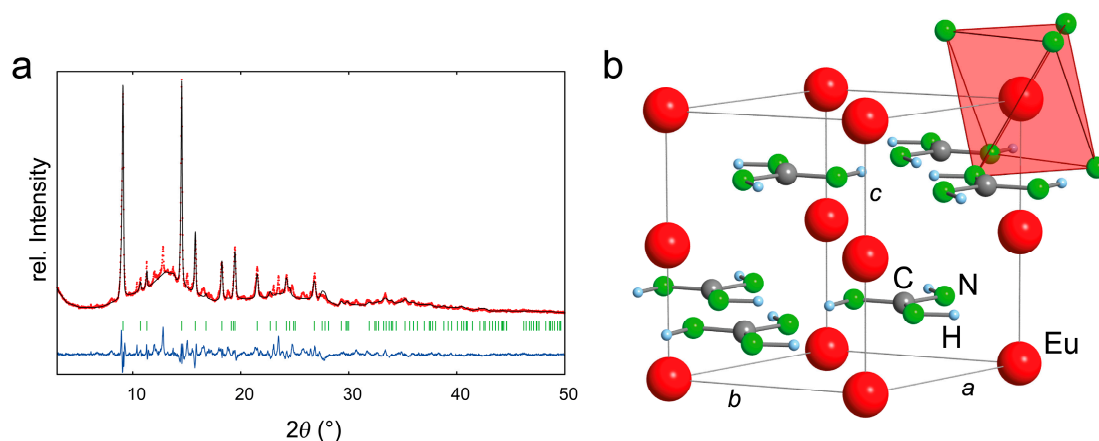
Figure 8. Rietveld refinement of EuC(NH)$_3$ (**a**), showing several unidentified reflections. The crystal structure of EuC(NH)$_3$ (**b**).

**Table 4.** Atomic positions and displacement parameters of EuC(NH)$_3$ in space group $P6_3/m$. Hydrogen position determined from DFT.

Atom	Wyckoff position	x	y	z	U_{iso} or U_{eq} (Å^2)
Eu	2b	0	0	0	0.058(1)
C	2c	1/3	2/3	1/4	0.005(7)
N	6h	0.065(4)	0.422(3)	1/4	0.005(7)
H (DFT)	6h	−0.092	0.486	1/4	–

Compared to both SrC(NH)$_3$ [30] and YbC(NH)$_3$ [31], EuC(NH)$_3$ shows a shorter *a*- and a longer *c*-axis, while the volume falls in-between the two. The C–N bonds are found to be somewhat short at 1.328(1) Å, close to a double bond although the bond order should be $1^1/_3$. As for the isostructural compounds, no hydrogen-bonding is expected.

The first magnetic measurements evidence ferromagnetic exchange interactions at low temperatures indicated by the occurrence of maxima in the μ_{eff} vs *T* curve (Figure 9), but without phase-pure samples, this result is only tentative. In particular, the μ_{eff} vs *T* curve for *T* > 25 K reveals, as for Eu(CN$_3$H$_4$)$_2$, ferromagnetic impurities that can be assigned to EuO and autoclave material. Furthermore, the unidentified side phase could be magnetic and contribute to the measured susceptibility.
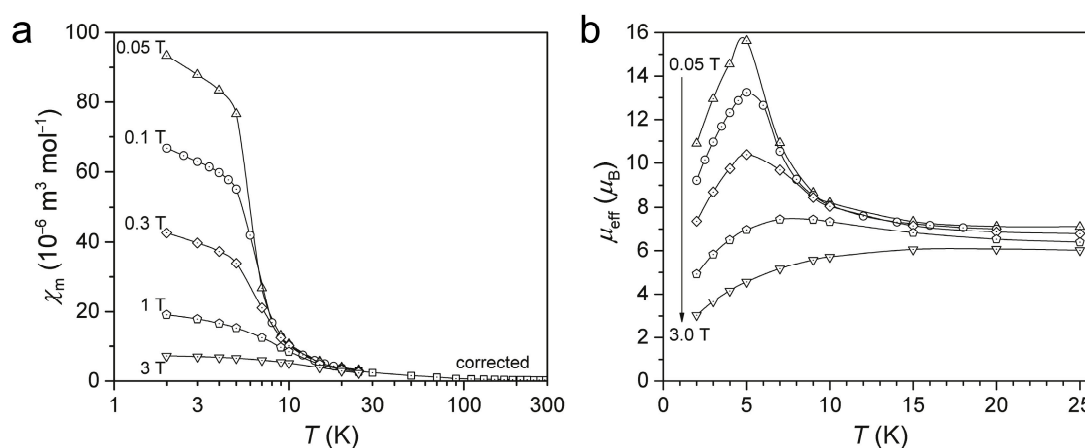
Figure 9. Magnetic susceptibility of EuC(NH)$_3$ vs temperature (**a**) and effective magnetic moment vs temperature (**b**), assuming molar weight of a pure EuC(NH)$_3$ sample (lines to guide the eye only).

3. Materials and Methods

3.1. Syntheses

The highly moisture-sensitive compounds were handled in an argon-filled glove box (MBRAUN, Garching, Germany) to prevent degradation. Reactants were used as obtained from the manufacturers mentioned below.

Guanidine CN$_3$H$_5$ was prepared in a one-pot synthesis in liquid ammonia in steel autoclaves as described in [31]. The autoclaves were constructed from stainless steel 1.4571 and a copper ring as a sealing gasket with a reaction volume of about 75 cm^3. A detailed description of the autoclaves can be found in [47].

Eu(CN$_3$H$_4$)$_2$ crystallizes in three different polymorphs, depending on the reaction temperature, as differentiated by PXRD. In all cases, stoichiometric reactants (0.2–1 mmol of Eu metal; Smart Elements, Vienna, Austria, 99.99%) were weighed in steel autoclaves and 15 cm^3 of dried, *solid* ammonia (Linde, Pullach, Germany, 99.999%, without further purification) were added. For the α-polymorph, compounds of highest crystallinity were obtained by heating for 5–10 days to 65 °C. β-Eu(CN$_3$H$_4$)$_2$ could be prepared by shorter reaction times of 2–5 days at only 50 °C, but higher quality and crystallinity could be obtained after the γ-polymorph converted to β-Eu(CN$_3$H$_4$)$_2$ (see below). γ-Eu(CN$_3$H$_4$)$_2$ was synthesized by reacting for 4–8 days at room temperature, sometimes yielding almost amorphous samples. During storage under argon, γ-Eu(CN$_3$H$_4$)$_2$ converted into β-Eu(CN$_3$H$_4$)$_2$ over the course of weeks, as evidenced from PXRD. All products showed traces of EuO (about 1 wt % from PXRD), most likely formed during handling of Eu metal in the glove box. Yields were 70%–80%. All Eu(CN$_3$H$_4$)$_2$ compounds were of a bright-yellow color.

EuC(NH)$_3$ was obtained from stoichiometric reactants (0.3–1 mmol of Eu) in steel autoclaves with 5–20 cm^3 of dried, solid ammonia. Reaction times were 4–14 days at 50–70 °C to yield 60%–80% of an orange powder. In some cases, however, only amorphous samples were obtained or EuC(NH)$_3$ was a product when Eu(CN$_3$H$_4$)$_2$ was targeted at suboptimal reaction conditions. Unfortunately, no phase-pure products could be achieved, but only mixtures with an unidentified side-phase (volume fraction estimated from PXRD 10%–20%).

3.2. Powder X-Ray Diffraction

For PXRD, the samples were sealed in 0.3 mm glass capillaries and measured with a STADI MP diffractometer (STOE, Darmstadt, Germany) with monochromatic Mo $K\alpha_1$ radiation and a Mythen detector. The measurement ranges were 3°–75° in 2θ with a step size of 0.015° for both EuC(NH)$_3$ and α-Eu(CN$_3$H$_4$)$_2$ and limited scans of 3°–21° in 2θ for γ- and β-Eu(CN$_3$H$_4$)$_2$. High-resolution synchrotron powder-diffraction data were collected using beamline 11-BM at the Advanced Photon Source (APS), Argonne National Laboratory using an average wavelength of 0.414170 Å. During the measurement, darkening of the samples was observed and the diffractograms were different from those obtained from our in-house diffractometer. Apparently, the samples decomposed under X-ray radiation, even more so when exposed to intense synchrotron radiation. For γ- and β-Eu(CN$_3$H$_4$)$_2$, similar loss in crystallinity was observed for long measurements with our in-house diffractometer, so limited scans were used for identification purposes.

The crystal structure of α-Eu(CN$_3$H$_4$)$_2$ was solved by charge-flipping with SUPERFLIP [48] as implemented in the Jana2006 suite [49] and further refined with the suite. To obtain a sensible structural model, the U_{iso} of the C and N atoms of each guanidinate unit were constrained. Also, the C–N distances, N–C–N angles, and CN$_3$ torsion angles were restrained to established values for the guanidinate unit as obtained from neutron-diffraction measurements [31,41]. Finally, a secondary phase of EuO [50] was added in the refinement, reaching a weight-percentage of 1.3(2) wt %.

The DFT-optimized structure of α-Eu(CN$_3$H$_4$)$_2$ in the experimental lattice parameters also describes the PXRD pattern well. In this Rietveld refinement, only the profile parameters—a single U_{iso} parameter for the Eu atoms, and another for all C and N atoms—were refined. These thermal displacement parameters were deposited with the calculated atomic positions as a CIF file.

For EuC(NH)$_3$, Rietveld refinements were performed with the Jana2006 suite using the reported SrC(NH)$_3$ structure type [30] as the starting model. The hydrogen atoms were located by DFT calculations (see below). All CIF data may also be obtained from FIZ Karlsruhe, 76344 Eggenstein-Leopoldshafen, Germany (fax: (+49)-7247-808-666; e-mail: crysdata@fiz-karlsruhe.de), on quoting the depository numbers CSD-432390 for α-Eu(CN$_3$H$_4$)$_2$ and CSD-432391 for EuC(NH)$_3$.

3.3. DFT Calculations

DFT calculations were computed at the PBE+D3(BJ)/PAW level [51–55] as implemented in VASP [56–59]. The cutoff energy for the plane-wave expansion was 500 eV; the *k*-meshes used for the calculations were sufficiently large. Phonon calculations did not use spin-polarization, and finite displacements of 0.01 Å were applied. The supercells for the phonon calculations of α-Eu(CN$_3$H$_4$)$_2$ and EuC(NH)$_3$ were 3 × 1 × 2 and 4 × 4 × 3, respectively. To arrive at hydrogen positions fitting our EuC(NH)$_3$ experimental results at 300 K, we started out from the latter and placed the hydrogen atoms as observed for SrC(NH)$_3$ [30] and YbC(NH)$_3$ [31]. Then, we selectively optimized the hydrogen positions, leaving lattice vectors and all other positions fixed. The resulting hydrogen positions are expected to be qualitatively comparable to those from neutron-diffraction experiments [46].

3.4. Magnetometry

Magnetic properties of both Eu(CN$_3$H$_4$)$_2$ and EuC(NH)$_3$ were measured with a superconducting quantum interference device (SQUID) magnetometer (MPMS-5XL, Quantum Design Inc., San Diego, CA, USA). Each polycrystalline sample was compacted and immobilized into cylindrical

polytetrafluoroethylene (PTFE) capsules. Measurements included field- and temperature-dependent molar magnetic susceptibilities (0.05–5.0 T, 2–290 K) and determination of the molar magnetization as a function of the applied field at 2 K. At applied fields of 0.1 T, the magnetic susceptibility was measured in field cooled (FC) and zero-field cooled (ZFC) mode, showing no significant difference. The data were corrected for diamagnetic contributions of sample holder and compound (Pascal's constants, $\chi_{dia} = -1.68 \times 10^{-9}$ m^3·mol^{-1}, $Eu(CN_3H_4)_2$ and -1.31×10^{-9} m^3·mol^{-1}, $EuC(NH)_3$).

Field-dependent measurements of the molar magnetic susceptibility χ_g allowed to correct for a small ferromagnetic impurity by applying the formula below for each temperature ($T > 20$ K) [10].

$$\chi_g(H) = \chi_g(\infty) + \frac{\sigma^s}{H}$$

For this formula, the magnetization must be a linear function of the field. Therefore, we included data of fields of up to 0.3 T to rule out errors caused by a saturation of α-$Eu(CN_3H_4)_2$ or $EuC(NH)_3$. Extrapolations to infinitely high fields yield the corrected values $\chi_m(\infty)$ through multiplying $\chi_g(\infty)$ by the molar mass of α-$Eu(CN_3H_4)_2$ or $EuC(NH)_3$.

3.5. IR Spectroscopy

An ALPHA FT-IR-spectrometer (Bruker, Billerica, MA, USA) placed in an argon-filled glove box and equipped with an ATR Platinum Diamond sample holder with a measurement range of $4000-400$ cm^{-1} was employed to measure the IR spectrum of $Eu(CN_3H_4)_2$. The results were compared to a DFT-based calculation of an IR spectrum of α-$Eu(CN_3H_4)_2$. The frequencies and eigenvectors at the $\mathbf{\Gamma}$-point were derived by a finite displacement approach as implemented PHONOPY [60], and the Born effective charge tensor was calculated by density-functional perturbation theory as implemented in VASP ("LEPSILON=.TRUE."). The IR intensities were derived from these values as described in references [33] and [34]. Also, a Gaussian broadening was applied to the spectrum.

4. Conclusions

In summary, we synthesized the α-, β- and γ-polymorphs of $Eu(CN_3H_4)_2$ and identified them by PXRD. The γ-phase transforms into the β-form over time. The IR spectra are dominated by the anion and are interpretable with the help of DFT calculations. Preliminary TGA measurements show that the guanidinates could be precursors for the preparation of (hydrogen) cyanamides. The crystal structure of α-$Eu(CN_3H_4)_2$ was solved by PXRD, and DFT was used to optimize the structural model. In α-$Eu(CN_3H_4)_2$, Eu is coordinated in double zigzag chains that are connected by the hydrogen-bonded guanidinate anions. The $CN_3H_4^-$ anions are predicted to adopt the *syn-*, *anti-*, and all-*trans*-conformations. The all-*trans*-conformation is found for the first time in a guanidinate. Magnetic measurements show paramagnetism at high temperatures and ferromagnetic exchange interactions below 6 K, presumably in one dimension along the Eu chains. Finally, $EuC(NH)_3$, isostructural to $SrC(NH)_3$ [30] and $YbC(NH)_3$ [31], is introduced as a possible low-temperature ferromagnet.

References

1. Abraham, D.S. The Next Resource Shortage? *The New York Times*, 20 November 2015.

2. Natural Environment Research Council. *Rare Earth Elements*; British Geological Survey: Nottingham, UK, 2011.

3. Zurawski, A.; Mai, M.; Baumann, D.; Feldmann, C.; Müller-Buschbaum, K. Homoleptic imidazolate frameworks $^3_\infty[Sr_{1-x}Eu_x(Im)_2]$-hybrid materials with efficient and tuneable luminescence. *Chem. Commun.* **2011**, *47*, 496–498. [CrossRef] [PubMed]

4. Rybak, J.-C.; Hailmann, M.; Matthes, P.R.; Zurawski, A.; Nitsch, J.; Steffen, A.; Heck, J.G.; Feldmann, C.; Götzendörfer, S.; Meinhardt, J.; et al. Metal–Organic Framework Luminescence in the Yellow Gap by Codoping of the Homoleptic Imidazolate $^3_\infty[Ba(Im)_2]$ with Divalent Europium. *J. Am. Chem. Soc.* **2013**, *135*, 6896–6902. [CrossRef] [PubMed]

5. Pust, P.; Weiler, V.; Hecht, C.; Tücks, A.; Wochnik, A.S.; Henß, A.-K.; Wiechert, D.; Scheu, C.; Schmidt, P.J.; Schnick, W. Narrow-band red-emitting $Sr[LiAl_3N_4]:Eu^{2+}$ as a next-generation LED-phosphor material. *Nat. Mater.* **2014**, *13*, 891–896. [CrossRef] [PubMed]

6. Kuda-Wedagedara, A.N.W.; Wang, C.; Martin, P.D.; Allen, M.J. Aqueous Eu^{II}-Containing Complex with Bright Yellow Luminescence. *J. Am. Chem. Soc.* **2015**, *137*, 4960–4963. [CrossRef] [PubMed]

7. Slabon, A.; Mensing, C.; Kubata, C.; Cuervo-Reyes, E.; Nesper, R. Field-Induced Inversion of the Magnetoresistive Effect in the Zintl Phase $Eu_{5+x}Mg_{18-x}Si_{13}$ (x = 2.2). *Angew. Chem. Int. Ed.* **2013**, *52*, 2122–2125. [CrossRef] [PubMed]

8. Rushchanskii, K.Z.; Kamba, S.; Goian, V.; Vaněk, P.; Savinov, M.; Prokleška, J.; Nuzhnyy, D.; Knížek, K.; Laufek, F.; Eckel, S.; et al. A multiferroic material to search for the permanent electric dipole moment of the electron. *Nat. Mater.* **2010**, *9*, 649–654. [CrossRef] [PubMed]

9. Niehaus, O.; Ryan, D.H.; Flacau, R.; Lemoine, P.; Chernyshov, D.; Svitlyk, V.; Cuervo-Reyes, E.; Slabon, A.; Nesper, R.; Schellenberg, I.; et al. Complex physical properties of EuMgSi—A complementary study by neutron powder diffraction and ^{151}Eu Mossbauer spectroscopy. *J. Mater. Chem. C* **2015**, *3*, 7203–7215. [CrossRef]

10. Lueken, H. *Magnetochemie: Eine Einführung in Theorie und Anwendung*; Teubner Verlag: Stuttgart, Leipzig, 1999.

11. Matthias, B.T.; Bozorth, R.M.; Van Vleck, J.H. Ferromagnetic Interaction in EuO. *Phys. Rev. Lett.* **1961**, *7*, 160–161. [CrossRef]

12. Kornblit, A.; Ahlers, G.; Buehler, E. Heat capacity of $RbMnF_3$ and EuO near the magnetic phase transitions. *Phys. Lett. A* **1973**, *43*, 531–532. [CrossRef]

13. Wachter, P. Europium chalcogenides: EuO, EuS, EuSe and EuTe. In *Handbook on the Physics and Chemistry of Rare Earths*; Elsevier: Amsterdam, The Netherlands, 1979; Volume 2, pp. 507–574.

14. Juza, R.; Hadenfeldt, C. Darstellung und Eigenschaften von Europium(II)-amid. *Naturwissenschaften* **1968**, *55*, 229. [CrossRef]

15. Hulliger, F. Ferromagnetism of europium amide $Eu(NH_2)_2$. *Solid State Commun.* **1970**, *8*, 1477–1478. [CrossRef]

16. Wickleder, C. $M(SCN)_2$ (M = Eu, Sr, Ba): Kristallstruktur, thermisches Verhalten, Schwingungsspektroskopie. *Z. Anorg. Allg. Chem.* **2001**, *627*, 1693–1698. [CrossRef]

17. Reckeweg, O.; DiSalvo, F.J. $EuCN_2$—The First, but Not Quite Unexpected Ternary Rare Earth Metal Cyanamide. *Z. Anorg. Allg. Chem.* **2003**, *629*, 177–179. [CrossRef]

18. Huppertz, H.; Schnick, W. $Eu_2Si_5N_8$ and $EuYbSi_4N_7$. The First Nitridosilicates with a Divalent Rare Earth Metal. *Acta Crystallogr. C* **1997**, *53*, 1751–1753. [CrossRef]

19. Höppe, H.A.; Trill, H.; Mosel, B.D.; Eckert, H.; Kotzyba, G.; Pöttgen, R.; Schnick, W. Hyperfine interactions in the 13 K ferromagnet $Eu_2Si_5N_8$. *J. Phys. Chem. Solids* **2002**, *63*, 853–859. [CrossRef]

20. Carrillo-Cabrera, W.; Somer, M.; Peters, K.; Schnering, H.G.V. Crystal structure of trieuropium bis(dinitridoborate), Eu$_3$[BN$_2$]$_2$. *Z. Kristallogr. New Cryst. Struct.* **2001**, *216*, 43–44. [CrossRef]

21. Liao, W.; Dronskowski, R. Carbodiimides with Extended Structures by an Azide-Cyanide Route: Synthesis and Crystal Structure of *M*$_2$Cl$_2$NCN (*M* = Eu and Sr). *Z. Anorg. Allg. Chem.* **2005**, *631*, 496–498. [CrossRef]

22. Stadler, F.; Oeckler, O.; Höppe, H.A.; Möller, M.H.; Pöttgen, R.; Mosel, B.D.; Schmidt, P.; Duppel, V.; Simon, A.; Schnick, W. Crystal Structure, Physical Properties and HRTEM Investigation of the New Oxonitridosilicate EuSi$_2$O$_2$N$_2$. *Chem. Eur. J.* **2006**, *12*, 6984–6990. [CrossRef] [PubMed]

23. Zucchi, G.; Thuéry, P.; Rivière, E.; Ephritikhine, M. Europium(II) compounds: Simple synthesis of a molecular complex in water and coordination polymers with 2,2′-bipyrimidine-mediated ferromagnetic interactions. *Chem. Commun.* **2010**, *46*, 9143–9145. [CrossRef] [PubMed]

24. Liao, W.; Hu, C.; Kremer, R.K.; Dronskowski, R. Formation of Complex Three- and One-Dimensional Interpenetrating Networks within Carbodiimide Chemistry: NCN^{2-}-Coordinated Rare-Earth-Metal Tetrahedra and Condensed Alkali-Metal Iodide Octahedra in Two Novel Lithium Europium Carbodiimide Iodides, LiEu$_2$(NCN)I$_3$ and LiEu$_4$(NCN)$_3$I$_3$. *Inorg. Chem.* **2004**, *43*, 5884–5890. [PubMed]

25. Yamada, T.; Liu, X.; Englert, U.; Yamane, H.; Dronskowski, R. Solid-State Structure of Free Base Guanidine Achieved at Last. *Chem. Eur. J.* **2009**, *15*, 5651–5655. [CrossRef] [PubMed]

26. Sawinski, P.K.; Meven, M.; Englert, U.; Dronskowski, R. Single-Crystal Neutron Diffraction Study on Guanidine, CN$_3$H$_5$. *Cryst. Growth Des.* **2013**, *13*, 1730–1735. [CrossRef]

27. Hoepfner, V.; Dronskowski, R. RbCN$_3$H$_4$: The First Structurally Characterized Salt of a New Class of Guanidinate Compounds. *Inorg. Chem.* **2011**, *50*, 3799–3803. [CrossRef] [PubMed]

28. Sawinski, P.K.; Dronskowski, R. Solvothermal Synthesis, Crystal Growth, and Structure Determination of Sodium and Potassium Guanidinate. *Inorg. Chem.* **2012**, *51*, 7425–7430. [CrossRef] [PubMed]

29. Sawinski, P.K.; Deringer, V.L.; Dronskowski, R. Completing a family: LiCN$_3$H$_4$, the lightest alkali metal guanidinate. *Dalton Trans.* **2013**, *42*, 15080–15087. [CrossRef] [PubMed]

30. Missong, R.; George, J.; Houben, A.; Hoelzel, M.; Dronskowski, R. Synthesis, Structure, and Properties of SrC(NH)$_3$, a Nitrogen-Based Carbonate Analogue with the Trinacria Motif. *Angew. Chem. Int. Ed.* **2015**, *54*, 12171–12175. [CrossRef] [PubMed]

31. Görne, A.L.; George, J.; van Leusen, J.; Dück, G.; Jacobs, P.; Chogondahalli Muniraju, N.K.; Dronskowski, R. Ammonothermal Synthesis, Crystal Structure, and Properties of the Ytterbium(II) and Ytterbium(III) Amides and the First Two Rare-Earth-Metal Guanidinates, YbC(NH)$_3$ and Yb(CN$_3$H$_4$)$_3$. *Inorg. Chem.* **2016**, *55*, 6161–6168. [CrossRef] [PubMed]

32. Jacobs, H.; Fink, U. Untersuchung des Systems Kalium/Europium/Ammoniak. *Z. Anorg. Allg. Chem.* **1978**, *438*, 151–159. [CrossRef]

33. Karhánek, D.; Bučko, T.; Hafner, J. A density-functional study of the adsorption of methane-thiol on the (111) surfaces of the Ni-group metals: II. Vibrational spectroscopy. *J. Phys. Condens. Matter* **2010**, *22*, 265006. [CrossRef] [PubMed]

34. Baroni, S.; de Gironcoli, S.; Dal Corso, A.; Giannozzi, P. Phonons and related crystal properties from density-functional perturbation theory. *Rev. Mod. Phys.* **2001**, *73*, 515–562. [CrossRef]

35. Hoepfner, V. Synthese und quantenchemische Untersuchung von Alkalimetallguanidinaten. Dissertation, RWTH Aachen University, Aachen, Germany, 2012.

36. Krott, M.; Liu, X.; Fokwa, B.P.T.; Speldrich, M.; Lueken, H.; Dronskowski, R. Synthesis, Crystal–Structure Determination and Magnetic Properties of Two New Transition-Metal Carbodiimides: CoNCN and NiNCN. *Inorg. Chem.* **2007**, *46*, 2204–2207. [CrossRef] [PubMed]

37. Liu, X.; Stork, L.; Speldrich, M.; Lueken, H.; Dronskowski, R. FeNCN and Fe(NCNH)$_2$: Synthesis, Structure, and Magnetic Properties of a Nitrogen-Based Pseudo-oxide and -hydroxide of Divalent Iron. *Chem. Eur. J.* **2009**, *15*, 1558–1561. [CrossRef] [PubMed]

38. Pöttgen, R.; Johrendt, D. Equiatomic Intermetallic Europium Compounds: Syntheses, Crystal Chemistry, Chemical Bonding, and Physical Properties. *Chem. Mater.* **2000**, *12*, 875–897. [CrossRef]

39. Van de Streek, J.; Neumann, M.A. Validation of experimental molecular crystal structures with dispersion-corrected density functional theory calculations. *Acta Crystallogr. B* **2010**, *66*, 544–558. [CrossRef] [PubMed]

40. Hoepfner, V.; Deringer, V.L.; Dronskowski, R. Hydrogen-Bonding Networks from First-Principles: Exploring the Guanidine Crystal. *J. Phys. Chem. A* **2012**, *116*, 4551–4559. [CrossRef] [PubMed]

41. Hoepfner, V.; Jacobs, P.; Sawinski, P.K.; Houben, A.; Reim, J.; Dronskowski, R. RbCN$_3$H$_4$ and CsCN$_3$H$_4$: A Neutron Powder and Single-Crystal X-ray Diffraction Study. *Z. Anorg. Allg. Chem.* **2013**, *639*, 1232–1236. [CrossRef]

42. Bailey, P.J.; Blake, A.J.; Kryszczuk, M.; Parsons, S.; Reed, D. The first triazatrimethylenemethane dianion: crystal structure of dilithio-triphenylguanidine Li$_2$[C(NPh)$_3$] as its tetrahydrofuran solvate. *J. Chem. Soc. Chem. Commun.* **1995**, 1647–1648. [CrossRef]

43. Bailey, P.J.; Mitchell, L.A.; Parsons, S. Guanidine anions as chelating ligands; syntheses and crystal structures of [Rh(η-C$_5$Me$_5$){η^2-(NPh)$_2$CNHPh}Cl] and [Ru(η-MeC$_6$H$_4$Pr^i-*p*)-{η^2-(NPh)$_2$CNHPh}Cl]. *J. Chem. Soc. Dalton Trans.* **1996**, 2839–2841. [CrossRef]

44. Shuskus, A.J. Electron Spin Resonance of Gd^{3+} and Eu^{2+} in Single Crystals of CaO. *Phys. Rev.* **1962**, *127*, 2022–2024. [CrossRef]

45. Baker, J.M.; Williams, F.I.B. Electron Nuclear Double Resonance of the Divalent Europium Ion. *Proc. R. Soc. A* **1962**, *267*, 283–294. [CrossRef]

46. Deringer, V.L.; Hoepfner, V.; Dronskowski, R. Accurate Hydrogen Positions in Organic Crystals: Assessing a Quantum-Chemical Aide. *Cryst. Growth Des.* **2011**, *12*, 1014–1021. [CrossRef]

47. Missong, R. Synthese und Charakterisierung von Strontium- und Bariumguanidinat. Dissertation, RWTH Aachen University, Aachen, Germany, 2016.

48. Palatinus, L.; Chapuis, G. SUPERFLIP—A computer program for the solution of crystal structures by charge flipping in arbitrary dimensions. *J. Appl. Cryst.* **2007**, *40*, 786–790. [CrossRef]

49. Petříček, V.; Dušek, M.; Palatinus, L. Crystallographic Computing System JANA2006: General features. *Z. Kristallogr.* **2014**, *229*, 345–352. [CrossRef]

50. McWhan, D.B.; Souers, P.C.; Jura, G. Magnetic and Structural Properties of Europium Metal and Europium Monoxide at High Pressure. *Phys. Rev.* **1966**, *143*, 385–389. [CrossRef]

51. Perdew, J.P.; Burke, K.; Ernzerhof, M. Generalized Gradient Approximation Made Simple. *Phys. Rev. Lett.* **1996**, *77*, 3865–3868. [CrossRef] [PubMed]

52. Grimme, S.; Antony, J.; Ehrlich, S.; Krieg, H. A consistent and accurate ab initio parametrization of density functional dispersion correction (DFT-D) for the 94 elements H–Pu. *J. Chem. Phys.* **2010**, *132*, 154104. [CrossRef] [PubMed]

53. Grimme, S.; Ehrlich, S.; Goerigk, L. Effect of the damping function in dispersion corrected density functional theory. *J. Comput. Chem.* **2011**, *32*, 1456–1465. [CrossRef] [PubMed]

54. Blöchl, P.E. Projector augmented-wave method. *Phys. Rev. B* **1994**, *50*, 17953–17979. [CrossRef]

55. Kresse, G.; Joubert, D. From ultrasoft pseudopotentials to the projector augmented-wave method. *Phys. Rev. B* **1999**, *59*, 1758–1775. [CrossRef]

56. Kresse, G.; Hafner, J. *Ab initio* molecular dynamics for liquid metals. *Phys. Rev. B* **1993**, *47*, 558–561. [CrossRef]

57. Kresse, G.; Hafner, J. *Ab initio* molecular-dynamics simulation of the liquid-metal–amorphous-semiconductor transition in germanium. *Phys. Rev. B* **1994**, *49*, 14251–14269. [CrossRef]

58. Kresse, G.; Furthmüller, J. Efficient iterative schemes for *ab initio* total-energy calculations using a plane-wave basis set. *Phys. Rev. B* **1996**, *54*, 11169–11186. [CrossRef]

59. Kresse, G.; Furthmüller, J. Efficiency of ab-initio total energy calculations for metals and semiconductors using a plane-wave basis set. *Comput. Mater. Sci.* **1996**, *6*, 15–50. [CrossRef]

60. Togo, A.; Tanaka, I. First principles phonon calculations in materials science. *Scr. Mater.* **2015**, *108*, 1–5. [CrossRef]